



PCCP

**Diffusion of Hydrophilic to Hydrophobic Forms of Nile Red in Aqueous C12EO10 Gels by Variable Area Fluorescence Correlation Spectroscopy**

Journal:	<i>Physical Chemistry Chemical Physics</i>
Manuscript ID	CP-ART-11-2022-005578.R1
Article Type:	Paper
Date Submitted by the Author:	03-Jan-2023
Complete List of Authors:	SHAFIEE, OMID; Kansas State University, Chemistry Jenkins, Samantha; Kansas State University, Department of Chemistry Ito, Takashi; Kansas State University, Department of Chemistry Higgins, Daniel; Kansas State University, Department of Chemistry

SCHOLARONE™  
Manuscripts

## **Diffusion of Hydrophilic to Hydrophobic Forms of Nile Red in Aqueous C<sub>12</sub>EO<sub>10</sub> Gels by Variable Area Fluorescence Correlation Spectroscopy**

*Omid Shafiee, Samantha G. Jenkins, Takashi Ito\* and Daniel A. Higgins\**

*Department of Chemistry, Kansas State University, 213 CBC Building, Manhattan, Kansas*

*66506-0401, USA*

### **ABSTRACT**

Solute diffusion within lyotropic liquid crystal gels prepared from a series of water and decaethylene glycol monododecyl ether (C<sub>12</sub>EO<sub>10</sub>) mixtures was explored by variable area fluorescence correlation spectroscopy. Aqueous C<sub>12</sub>EO<sub>10</sub> gels were prepared in concentrations ranging from 55:45 to 70:30 wt% of surfactant and water. Small angle X-ray scattering revealed that these gels comprise hexagonal mesophases of cylindrical micelles. Micelle spacing was found to decrease with increasing C<sub>12</sub>EO<sub>10</sub> concentration. Three different Nile red (NR) dyes were employed as model solutes and were separately doped into the gels at nanomolar levels. These include a hydrophilic form of NR incorporating an anionic sulfonate group (NRSO<sub>3</sub><sup>-</sup>), a hydrophobic form incorporating a fourteen-carbon alkane tail (NRC<sub>14</sub>), and commercial NR as an intermediate case. FCS data acquired from the gels revealed that NRSO<sub>3</sub><sup>-</sup> diffused primarily in 3D. Its diffusion coefficient exhibited a monotonic decrease with increasing gel concentration and micelle packing density, consistent with confinement of its motions by its exclusion from the micelle cores. NRC<sub>14</sub> exhibited the smallest diffusion coefficient, most likely due to its larger size and enhanced interactions with the micelle cores. NR yielded an intermediate diffusion coefficient and the most anomalous behavior of the three dyes, attributable to its facile partitioning between core and corona regions, and greater participation by 1D diffusion. The results of these studies afford an improved understanding of molecular mass transport through

\*Corresponding author emails: [ito@ksu.edu](mailto:ito@ksu.edu) and [higgins@ksu.edu](mailto:higgins@ksu.edu)

soft-matter nanomaterials like those being developed for use in drug delivery and membrane based chemical separations.

## Keywords

Fluorescence correlation spectroscopy diffusion law, surfactant mesophases, nanoconfinement, mass transport mechanisms, single molecule detection

## Introduction

Nanostructured lyotropic liquid crystals (LLCs) derived from nonionic surfactants find myriad potential applications in controlled drug release,<sup>1-3</sup> chemical separations,<sup>4,5</sup> and in the templated synthesis of nanomaterials.<sup>6,7</sup> The concentration-dependent structures and organization of many such materials have been explored by X-ray<sup>8,9</sup> and neutron scattering,<sup>10,11</sup> by nuclear magnetic resonance spectroscopy,<sup>10</sup> by polarized light microscopy,<sup>9,12</sup> and by cryogenic transmission electron microscopy.<sup>13,14</sup> However, the optimization of LLCs for many of their applications also requires knowledge of the mass transport dynamics exhibited by solutes confined within them. Far fewer studies have explored these phenomena, and much less is known about how organized, crowded nonionic LLC nanostructures either facilitate or limit solute diffusion. Relevant prior work in this area includes radio tracer,<sup>15</sup> and Taylor Dispersion<sup>16,17</sup> studies of diffusion by both surfactants and probes in relatively dilute micellar solutions. Interestingly, pulsed-field gradient NMR studies have revealed anisotropic diffusion caused by aligned LLC nanostructures<sup>18,19</sup> in more concentrated systems.

Optical microscopic methods offer valuable alternative routes to exploring the rates and mechanisms of solute mass transport in LLCs. Fluorescence correlation spectroscopy (FCS)<sup>20-22</sup> represents a particularly useful method in this regard, having been employed previously to study

diffusion in a variety of biologically- and technologically-relevant materials.<sup>23-26</sup> In FCS, a confocal microscope is employed to illuminate a diffraction-limited region of the sample. The sample is doped at low (i.e., pM - nM) concentrations with a luminescent dye so that only a few molecules are present within the detection volume at any instant in time. These molecules diffuse in and out of the detection region, producing fluorescence fluctuations that are easily recorded. Subsequent autocorrelation of the fluorescence time transients obtained allows for determination of the molecular concentration, the average residence time of the molecules in the confocal volume, and their diffusion coefficient,  $D$ .

FCS experiments are commonly performed using a detection region of fixed size. Unfortunately, this restriction may prevent full characterization of the diffusion mechanism by masking any variations that occur on sub-micron length scales. To overcome this limitation, variable area FCS (va-FCS) measurements are now regularly employed.<sup>27-29</sup> In its most common form, va-FCS employs confocal methods in which the illumination and detection regions are simultaneously varied in size. For Fickian diffusion, the measured diffusion time,  $\tau_D$ , is expected to be linearly dependent on detection area (or volume), yielding a zero intercept when the data are extrapolated to zero area. The observation of an affine dependence of  $\tau_D$  (i.e., a non-zero intercept) provides evidence of deviations from Fickian behavior due to confinement by the material structure.<sup>28-30</sup> However, such deviations are difficult to detect in samples with features much smaller than the diffraction limit, unless they cause significant slowing of probe molecule diffusion.<sup>31</sup>

In this manuscript, we employ va-FCS to explore the rates and mechanisms of solute diffusion for a series of organic dyes dissolved within polyoxyethylene alkyl ether derived LLC mesophases. The dyes are all derivatives of Nile red (NR)<sup>32,33</sup> and are sufficiently fluorescent to

be detected at the single molecule level. The commercial form of NR is employed along with a more hydrophilic, anionic form incorporating a sulfonate group ( $\text{NRSO}_3^-$ ) and a hydrophobic form incorporating a fourteen-carbon-long alkane tail ( $\text{NRC}_{14}$ ). Decaethylene glycol monododecyl ether ( $\text{C}_{12}\text{EO}_{10}$ ) was employed to form the LLCs.<sup>12,34</sup> When mixed with water at appropriate concentrations, this commercially available surfactant readily forms highly viscous, optically-transparent gels comprising a hexagonal phase of cylindrical micelles. These gels may incorporate micelles a few hundred nanometers in length<sup>13,14</sup> or other heterogeneities that limit solute diffusion on length scales accessible by diffraction-limited va-FCS methods. Small angle X-ray scattering data are used to verify the formation of the hexagonal mesophase and to quantitatively determine micelle spacing across a range of surfactant concentrations. The results obtained from va-FCS studies are used to quantitatively determine the diffusion coefficient of each dye, to explore its mass transport mechanism, and to obtain possible evidence that its diffusion is confined by the material nanostructure.

## Experimental

**Materials.** Decaethylene glycol monododecyl ether ( $\text{C}_{12}\text{EO}_{10}$ ) (see Figure 1a) was obtained from Sigma-Aldrich and was used as received. LLC gels were prepared as aqueous solutions and were obtained by first weighing an appropriate amount of  $\text{C}_{12}\text{EO}_{10}$  into a disposable glass vial. The necessary amount of pure water (Barnstead B-pure, 18 M $\Omega$  cm) was then added to bring the total mass of the gel to 2 g. This was followed by the addition of a 50  $\mu\text{L}$  aliquot of one of the three dyes (see below) as a 0.8  $\mu\text{M}$  ethanol solution, bringing the final dye concentration in each gel to  $\sim 20$  nM. A series of gels having compositions ranging from 55:45 wt% up to 70:30 wt% were employed in optical experiments. After addition of the dye, the vials were tightly sealed and the gels thoroughly mixed by repeated inversion and centrifugation.

Mixing was facilitated by heating the gels to 60 - 70 °C to reduce their viscosity. As a final step, they were centrifuged for ~ 1 h to obtain optically clear gels that were free of visible air bubbles. The gels were stored for a minimum of one day in the dark prior to use.

Nile red (NR) was obtained from Sigma-Aldrich and was used as received. Hydrophilic and hydrophobic derivatives of NR were obtained by modifying a hydroxylated form of Nile red previously synthesized in our labs.<sup>35</sup> The structures of all three dyes are shown in Figure 1b. The hydrophobic form of the dye incorporated a fourteen-carbon-long n-alkyl ether tail (NRC<sub>14</sub>) while the hydrophilic form was obtained as a sulfonated n-propyl ether derivative (NRSO<sub>3</sub><sup>-</sup>). Descriptions of the synthesis, purification, and characterization of NRC<sub>14</sub> and NRSO<sub>3</sub><sup>-</sup> are provided in ESI†.

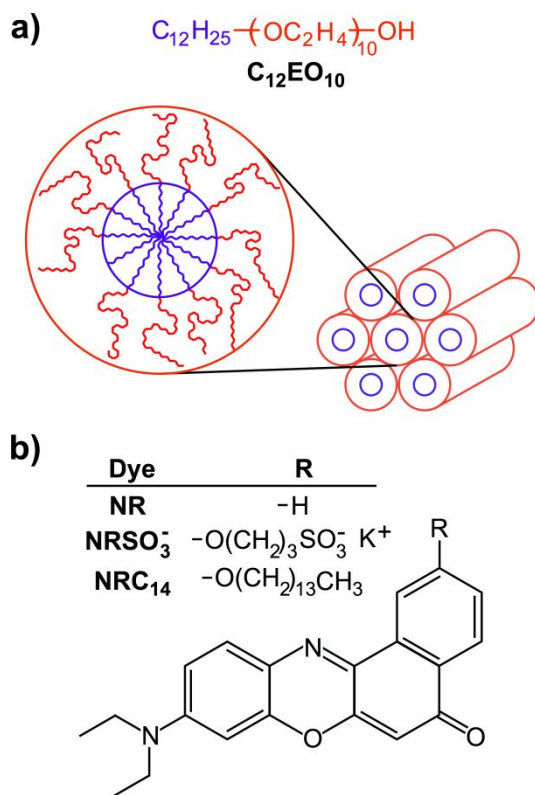


**Figure 1.** **a)** Molecular structure of C<sub>12</sub>EO<sub>10</sub>, cross-section of cylindrical micelle structure showing the core (inner blue circle) and corona (outer red circumference) regions, and the hexagonal arrangement of micelles. **b)** NR dyes employed as model solutes within C<sub>12</sub>EO<sub>10</sub> gels.

**Methods.** Small angle X-ray scattering (SAXS) experiments were performed on a Xenocs Ganesha SAXS at the University of Minnesota CharFac. This instrument employs a Cu-K $\alpha$  X-ray source. Scattered X-rays were detected using an Eiger 1M (Dectris) position sensitive detector. Samples were prepared for these measurements by first warming the gels to 60 - 70 °C and subsequently loading them into 1 mm diameter boron-rich thin-walled (0.01 mm wall thickness) glass capillaries (Charles Supper) under mild vacuum. Afterwards, the capillaries were sealed with paraffin wax to prevent evaporation of the water. The samples were maintained at ambient temperature under atmospheric pressure during all SAXS measurements. SAXS data were integrated for 300 – 900 s in each experiment.

Variable area fluorescence correlation spectroscopy (va-FCS) data were acquired on a sample-scanning confocal microscope that was modified from its previously-described configuration.<sup>36</sup> Briefly, the confocal microscope is built upon an inverted fluorescence microscope (Nikon TE-300). It employs an oil immersion objective (Nikon Plan Fluor, 100X, 1.3 NA) for illumination of the sample and for collection of fluorescence emitted by the dye. A single photon counting avalanche photodiode (APD, Perkin Elmer SPCM-AQ-141R) was used to detect the fluorescence. Light from a solid-state laser (Coherent Verdi-5W, 532 nm) was used to excite the dye. The laser light was first directed through a telescope to reduce the beam diameter to  $\sim 530 \mu\text{m}$  full-width-at-half-maximum so that it under-filled the back aperture of the oil immersion objective. Under-filling of the objective ensured that a region in the sample a few microns ( $\sim 2.5 \mu\text{m}$ ) in diameter was illuminated for va-FCS experiments. The laser light was directed into the microscope objective by reflection from a dichroic beamsplitter (Chroma, 550 DCLP). An incident power of 50  $\mu\text{W}$  was typically employed in experiments performed on LLC

gels, while 5-10  $\mu\text{W}$  was employed for measurements in pure solvents. The power in each case was measured prior to reflection from the beamsplitter.

Each sample was mounted above the microscope objective within a custom-made cell comprised of a perforated glass slide sandwiched between two microscope coverglasses (FisherFinest, Premium). The gels were transferred into these cells after warming them to 60 - 70  $^{\circ}\text{C}$ . They were subsequently allowed to cool to room temperature and sealed prior to mounting on the microscope. Unlike previous studies of related materials,<sup>37,38</sup> this cell design was not expected to produce well-aligned hexagonal LLCs. Fluorescence was excited in each gel by focusing the incident laser at a distance of  $\sim 5 \pm 1 \mu\text{m}$  above the lower coverglass, within the dye-doped gel. The focus was maintained at this position throughout all va-FCS experiments to avoid variations in the FCS results caused by spherical aberrations.<sup>39-41</sup>

Fluorescence from the detection volume was collected by the aforementioned objective, passed back through the dichroic beamsplitter, and focused by the internal tube lens of the microscope into a pinhole positioned in its primary image plane. The pinhole employed in each experiment was selected from a series of pinholes on a pinhole wheel (ThorLabs). These pinholes had diameters of 70, 80, 90, 100, and 125  $\mu\text{m}$ . Selection of the different pinhole sizes allowed for the detection area within the sample to be systematically varied. Note that this allows for systematic variation of both the lateral and longitudinal dimensions of the detection region. In contrast, the size of the excitation region was held constant, as has been done previously in imaging FCS experiments.<sup>29</sup> After passage through the pinhole, the fluorescence was sent through an appropriate bandpass filter (Chroma) having a passband centered at 640 nm and a bandwidth of  $\pm 20$  nm. Finally, the fluorescence was focused onto the photosensitive surface of the APD detector. Individual photon pulses from the APD were counted using a



National Instruments counter/timer board (PCIe-6612) configured to operate in the time-stamping mode.<sup>42</sup> Either a 10 MHz or 25 MHz clock was used as the timer for time stamping. The data obtained were used to prepare a series of time transients having bin times of  $\geq 10^{-6}$  s. The transients were subsequently processed to obtain autocorrelation functions using C++ and Igor Pro routines written in house. A total of five to ten replicate data sets were acquired from each position within each of the samples over the course of 25 min in each experiment. The individual replicate decays were averaged together to obtain the autocorrelation functions used in the assessment of diffusion rates and mechanisms.

## Results and Discussion

**Characterization of C<sub>12</sub>EO<sub>10</sub> Gel Nanostructure.** Representative SAXS data obtained from a 62.5 wt% C<sub>12</sub>EO<sub>10</sub> gel are shown in Figure 2 (inset). Three peaks are found at  $q = 1.268$  nm<sup>-1</sup>, 2.202 nm<sup>-1</sup>, and 2.522 nm<sup>-1</sup> in these data. These are assigned to the 10, 11, and 20 Bragg reflections, respectively, of a hexagonal LLC mesophase of cylindrical C<sub>12</sub>EO<sub>10</sub> micelles.<sup>43</sup> The

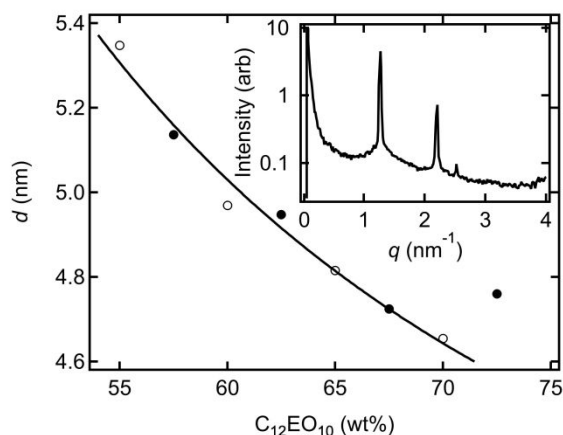


**Figure 2.** Mean SAXS  $d$  spacing as a function of gel composition for two series of samples prepared on different days (open and filled circles). The inset shows representative SAXS data obtained from a 62.5 wt% C<sub>12</sub>EO<sub>10</sub> aqueous gel (300 s integration). The solid line shows a fit revealing the quadratic dependence of  $d$  spacing on surfactant concentration across much of the range investigated.

2D SAXS pattern from which these data were derived is provided in ESI† (Figure S5) and reveals that the cylindrical micelles were oriented parallel to the long axis of the glass capillary containing the gel.

Figure 1a shows a model for the arrangement of  $C_{12}EO_{10}$  molecules within the cylindrical micelles, and for hexagonal arrangement of the micelles in the gels. The  $C_{12}EO_{10}$  monomer includes a long hydrophilic ethylene oxide segment and a shorter hydrophobic alkane tail. Within the micelles, the alkane segments comprise the nonpolar micelle core, as shown in blue in Figure 1a, while the ethylene oxide segments form the more polar corona region, as shown in red.<sup>10</sup> The micelle core is estimated to be  $\sim 2.4$  nm in diameter based on the fully extended length of the alkane segments, while the corona comprises the remainder of the micelle volume.

Micelle spacing was determined from the 10 Bragg peak, which yields a  $d$  spacing of 4.96 nm and a lattice  $a$  parameter of 5.72 nm for the 62.5 wt% gel (Figure 2 inset). The distance between micelles was found to decrease with increasing gel concentration. Figure 2 plots  $d$  as a function of concentration for two separate series of samples prepared on different days at 55, 60, 65, and 70 wt%  $C_{12}EO_{10}$  and 57.5, 62.5, 67.5, and 72.5 wt%  $C_{12}EO_{10}$ , respectively. The surfactant concentrations employed are all well above the critical micelle concentration of  $\sim 0.10$  mM.<sup>10,44</sup> All gels in this range were highly viscous at room temperature and exhibited no evidence of flow over long periods of time.

Although a detailed phase diagram for  $C_{12}EO_{10}$  in water has apparently not yet been reported, phase diagrams for closely related gels (i.e.  $C_{12}EO_8$ <sup>12</sup> and  $C_{12}EO_{12}$ <sup>9</sup>) have appeared, suggesting a hexagonal phase should be found near the range of concentrations investigated. Indeed, SAXS data acquired from all gels between 55 wt%  $C_{12}EO_{10}$  and 70 wt%  $C_{12}EO_{10}$  included both 10 and 11 Bragg peaks (data not shown), consistent with hexagonally arranged

cylindrical micelles in each case. Data acquired at concentrations above 70 wt% C<sub>12</sub>EO<sub>10</sub> exhibited only a single Bragg peak, suggesting a change in phase at higher concentrations.

The trend in  $d$  spacing shown in Figure 2 is consistent with a C<sub>12</sub>EO<sub>10</sub> concentration-dependent increase in micelle packing density. The surfactant aggregation number, and hence, full micelle diameter, likely remain approximately constant across the range of concentrations employed, as has been reported previously.<sup>11</sup> Indeed, a more detailed analysis of the SAXS data reveals an approximately quadratic decrease in  $d$  with increasing C<sub>12</sub>EO<sub>10</sub> concentration (see fit in Figure 2), as expected for a concentration-dependent change in micelle packing density. The only deviation from this trend occurred at > 70 wt% C<sub>12</sub>EO<sub>10</sub>, possibly due to the aforementioned phase transition in the LLC. As a result, the investigations described below were restricted to gels of  $\leq 70$  wt% surfactant.

The width of the 10 Bragg peak was also used to determine the correlation length of the organized structures within the gels. The full-width-at-half-maximum (FWHM) was estimated in each case by fitting the diffraction peaks (see Figure 2) to a Gaussian. The correlation length was calculated as  $2\pi/\text{FWHM}$ , assuming negligible contributions to the width from instrumental broadening. No clear trend was observed as a function of gel concentration. The average correlation length obtained across the range of concentrations investigated was  $170 \text{ nm} \pm 90 \text{ nm}$ , indicating that the LLCs form domains that remain ordered, on average, over this length scale.

**Fluorescence Time Transients and Autocorrelation Functions.** The fluorescence time stamping data were used to construct time transients and autocorrelation functions spanning more than six orders of magnitude in time from 1  $\mu$ s to 3 s. Figure 3 shows representative time transients obtained from a 60:40 C<sub>12</sub>EO<sub>10</sub> gel doped with 20-nM NR dye. These show strong fluorescence fluctuations due to diffusion of dye molecules through the confocal detection region. As expected, the average signal level increases and the time scale over which the

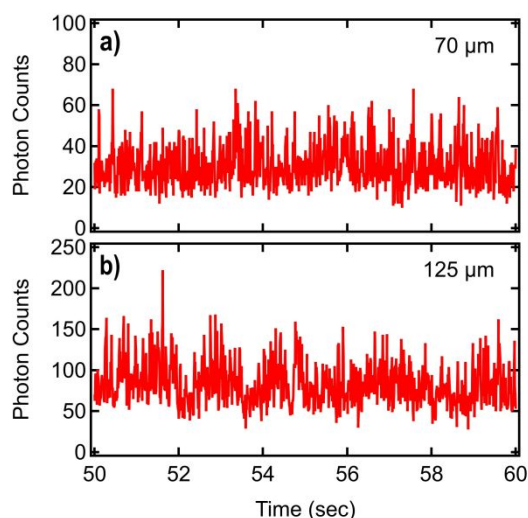


**Figure 3.** Representative segments of time transient data obtained from 20 nM NR in a 60:40 C<sub>12</sub>EO<sub>10</sub> gel using **a)** 70  $\mu$ m and **b)** 125  $\mu$ m diameter pinholes. These time transients are plotted with 10 ms bin times.

fluctuations occur becomes longer with increasing pinhole size. The equation used in autocorrelating the data is given as Eq. 1.

$$G(\tau) = \frac{\langle F(t)F(t+\tau) \rangle}{\langle F(t) \rangle^2} - 1 \quad (\text{Eq. 1})$$

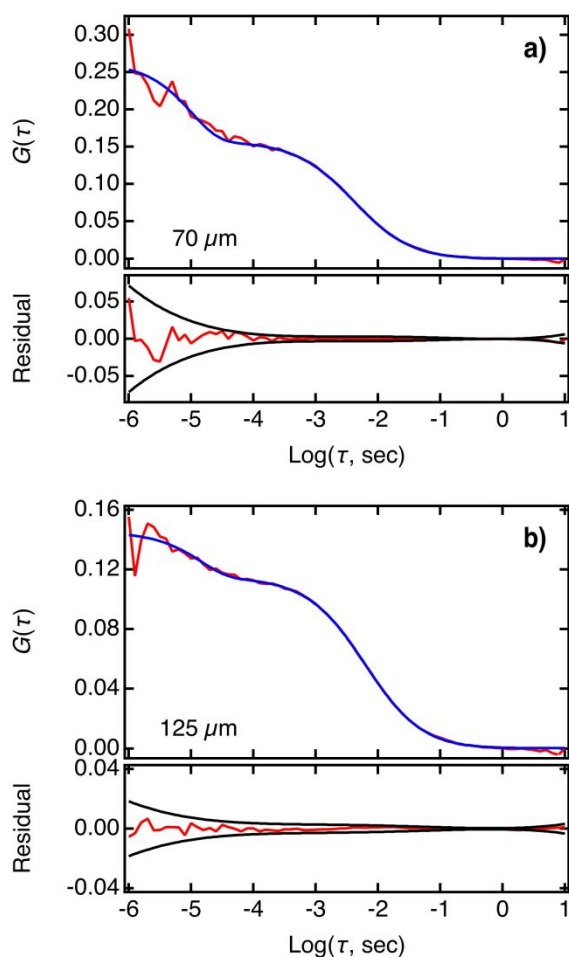


**Figure 4.** Representative FCS data (red lines) obtained from 20 nM NR in a 60:40  $C_{12}EO_{10}$  aqueous gel using **a)** 70  $\mu\text{m}$  and **b)** 125  $\mu\text{m}$  pinholes. The FCS data depict the average of five replicate decays. Also shown are their fits (blue lines) to the model given in Eq. 2. The fitting residuals (red lines) and estimated 95% confidence intervals (black lines) derived from the five replicate decays are plotted below each data set.

Here,  $F(t)$  represents the time transient at a given time resolution, and  $F(t+\tau)$  is a copy of the same, but delayed by time  $\tau$ . The triangular brackets indicate the time-averaged value is determined. Figure 4 plots  $G(\tau)$  for two representative data sets.

The autocorrelation functions reveal that the fluorescence fluctuations occur on two distinct timescales, producing decays near  $\sim 10 \mu\text{s}$  and  $\sim 10 \text{ms}$ . The  $10 \mu\text{s}$  fluctuations are too fast to arise from translational diffusion of the dye within the gels. While the fast component is

accounted for in fitting the autocorrelation decays (see below), its origins are not relevant to the present studies and are not explored further. The fluctuations occurring in the  $\sim 10$  msec range are attributed to diffusion of the dye through the gels and are the sole focus of this study.

The autocorrelation decays afford valuable information on both the rates and mechanisms of dye diffusion. A model that properly describes the diffusion mechanism will afford a good fit to the autocorrelation function, while an incorrect model may not. As it may be possible to fit the data to more than one model, other evidence is usually required to properly assign the diffusion mechanism. According to both the SAXS data obtained in these studies (Figure 2), and the results of earlier reports,<sup>8,37</sup> dye diffusion may be confined to one dimension (1D) by the hexagonally arranged cylindrical micelles of the  $C_{12}EO_{10}$  gels. However, as discussed in ESI†, all three Nile red dyes appear to be associated with similar environments of relatively high polarity (on average). These results suggest they readily partition between the micelle core and corona regions, implying variable contributions from 1D and 3D dye diffusion to the observed fluorescence fluctuations. Indeed, attempts to fit the autocorrelation functions to a model for pure 1D diffusion proved unsatisfactory. Attempts to fit the data to a multicomponent model including both 1D and 3D diffusion yielded highly variable component amplitudes and diffusion times. As a result of these difficulties, a model for anomalous 3D diffusion (Eq. 2) was instead employed.

$$G(\tau) \approx A + \frac{1}{N} \left[ B \left( \frac{1}{1 + (\tau/\tau_D)^\alpha} \right) \left( \frac{1}{1 + (\tau/\tau_D)^\alpha (1/\gamma^2)} \right)^{1/2} + C e^{-k\tau} \right] \quad (\text{Eq. 2})$$

Here,  $A$ ,  $B$ , and  $C$  are constants defining the contributions of a fixed offset and the amplitudes of the slow and fast fluctuations mentioned above.  $N$  is the average number of molecules in the detection region, and  $k$  is the rate constant for the fast ( $\sim 10$   $\mu$ s) fluctuations. The dye diffusion time is given by  $\tau_D = \omega_r^2/4D$ , where  $D$  is its diffusion coefficient,  $\omega_r$  is the calibrated radius of

the detection region and  $\gamma = \omega_a/\omega_r$ . In the latter,  $\omega_a$  represents the axial dimension of the detection region. The values employed for  $\omega_r$  were quantitatively measured at each pinhole size, as described in ESI†. The value of  $\gamma$  was determined to be  $\sim 4$  from theory, and similar values are reported in the literature.<sup>41</sup> Finally,  $\alpha$  describes the occurrence of anomalous diffusion, with  $\alpha = 1$  for Brownian diffusion in 3D and  $\alpha < 1$  for anomalous sub-diffusion. In these studies, as the dyes were expected to exhibit a combination of 1D and 3D diffusion, values of  $\alpha < 1$  were interpreted to reflect the broadening of the autocorrelation decays by the simultaneous occurrence of 1D and 3D dye diffusion. It should be noted that the approximation in Eq. 2 is valid when  $\tau_D \gg 1/k$ ,<sup>45</sup> as is the case in these studies, in which the timescales of fast and slow fluorescence fluctuations differed by a factor of  $\sim 10^3$ .

Figure 4 shows representative fits of the autocorrelation data to Eq. 2. The data were fit from  $10^{-6}$  s to 3 s. The residuals for each fit are shown below each autocorrelation function. The black lines plotted with the residuals show the estimated 95% confidence intervals. Raw confidence intervals were obtained from the standard deviations of the five replicate decays used to produce the average autocorrelation decays shown. They were subsequently fit to polynomials and the latter are shown as the confidence intervals in Figure 4. The residuals all fall predominantly within the 95% confidence intervals, demonstrating the goodness of the fits to Eq. 2. All FCS data for the three dyes were found to fit best to Eq. 2, in comparison to the aforementioned alternatives, as judged by the fitting residuals.

Although all autocorrelation data from the gels could be fit well to Eq. 2, subtle differences in the decays were detected for the three dyes at the different gel concentrations. These imply variations in the molecular-level details of their diffusion mechanisms. In assessing the dye diffusion behaviors, differences in their  $\alpha$  values were considered first. The values obtained for

all three dyes were found to be independent of pinhole size. Figure 5a plots their average values as a function of  $C_{12}EO_{10}$  concentration. NR yielded the smallest  $\alpha$  values of the three dyes. In contrast,  $NRSO_3^-$  yielded the largest  $\alpha$  values at all but the highest gel concentration, while  $NRC_{14}$  exhibited intermediate behavior. The  $\alpha$  values obtained from NR and  $NRSO_3^-$  in homogeneous glycerin-ethanol mixtures have been included for comparison and are plotted on the right side of Figure 5a. Fitting of the data from both of these controls yielded  $\alpha = 1$  within experimental error. Data from  $NRC_{14}$  in the same glycerin-ethanol mixture appeared to be limited by its low solubility and are not included as a result.

While the exact origins of the smaller  $\alpha$  values obtained from NR in the gels remain unknown, it is believed they reflect its greater partitioning into the micelle core regions, and hence, greater contributions of 1D diffusion to its motion. In contrast, the larger values obtained from  $NRSO_3^-$  suggest it spends relatively more time in the polar corona regions where it can diffuse in 3D. While  $NRC_{14}$  was expected to associate most strongly with the micelle cores, its larger size may prevent it from penetrating the core regions, resulting in its intermediate behavior. In this latter case, transient association of  $NRC_{14}$  with the micelle cores may slow its motion while not producing clear 1D diffusion. No clear dependence of  $\alpha$  on  $C_{12}EO_{10}$  concentration was observed for any of the dyes (see Figure 5a). Therefore, the dimensionality of dye diffusion is believed to be largely independent of micelle packing density at the gel concentrations investigated.



Differences in the dye diffusion mechanisms were further revealed by their diffusion

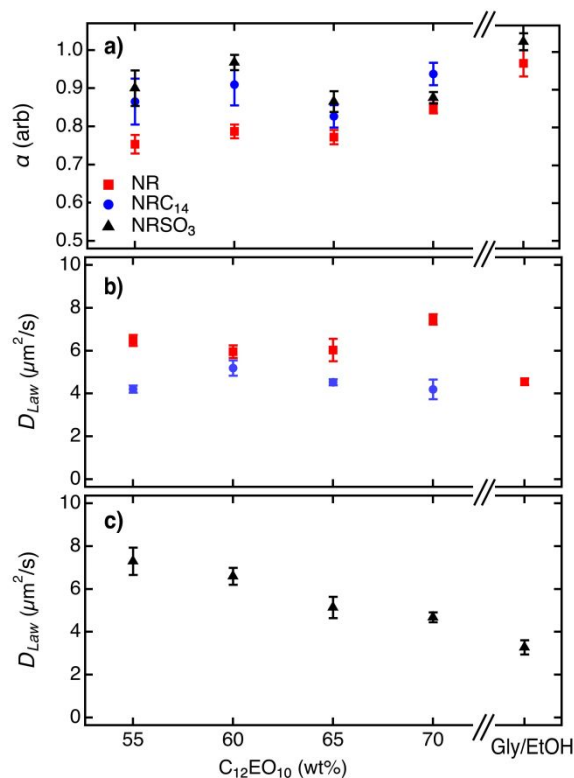


**Figure 5.** **a)** Mean  $\alpha$  values (Eq. 2), and **b), c)** mean diffusion coefficients,  $D_{Law}$ , determined by fitting diffusion law plots like those in Figure 6 to Eqn. 3 (with  $\tau_0 = 0$ ) for the three dyes at each  $C_{12}EO_{10}$  concentration. The data points plotted on the right of each graph were obtained from homogeneous glycerin-ethanol mixtures (75:25). The  $\alpha$  values are averaged across all pinhole sizes. The error bars depict the 95% confidence intervals.

coefficients. The latter were obtained by plotting the  $\tau_D$  values from fits to Eq. 2 against  $\omega_r^2$ , as shown in Figure 6. These plots were subsequently fit to the well-known diffusion law equation, to obtain quantitative measures of  $D_{Law}$ .<sup>28,29,46</sup>

$$\tau_D = \tau_0 + \frac{\omega_r^2}{4D_{Law}} \quad (\text{Eq. 3})$$

Here,  $\omega_r^2$  is the calibrated area of the detection region, and  $\tau_0$  is the intercept of fitted line.

Fickian diffusion is expected to yield  $\tau_0 = 0$ , while domain confined diffusion would yield  $\tau_0 >$

0.<sup>28,29,46</sup>

Confinement of dye diffusion by sub-micron-sized nanostructures has been detected previously in biological samples by diffusion-law analyses like those shown in Figure 6, using Eq. 3.<sup>27,28</sup> Although the lateral dimensions and spacings of the C<sub>12</sub>EO<sub>10</sub> micelles are much

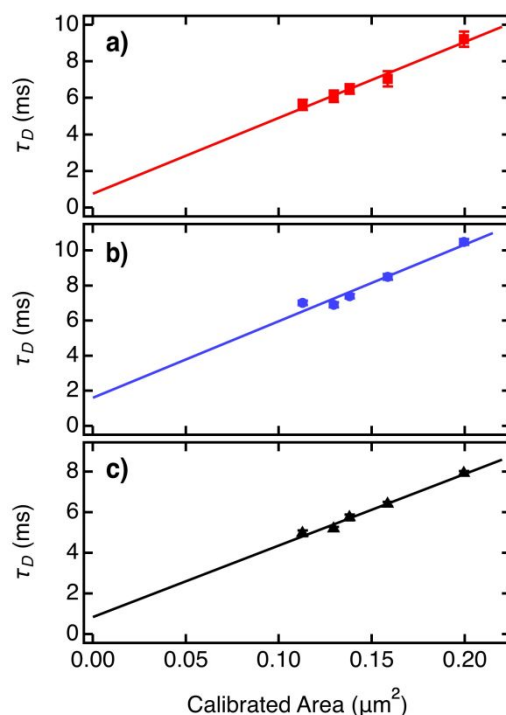


**Figure 6.** Representative diffusion times,  $\tau_D$ , as a function of calibrated detection area for **a)** NR (red squares), **b)** NRC<sub>14</sub> (blue circles), and **c)** NRSO<sub>3</sub><sup>-</sup> (black triangles) in 60:40 C<sub>12</sub>EO<sub>10</sub> gels. All suggest diffusion occurs by a Fickian mechanism. Pinholes of 70, 80, 90, 100, and 125  $\mu\text{m}$  diameters were employed. The solid lines depict fits of the data to Eq. 3 allowing  $\tau_0 \neq 0$ . Error bars depict 95% confidence intervals on the autocorrelation fitting parameters.

smaller than the diffraction-limited resolution of the optical microscope employed, the micelles are expected to be a few hundred nanometers in length,<sup>13,14</sup> and could therefore yield evidence for domain confined diffusion on similar length scales. Unfortunately, a quantitative statistical test for deviations of diffusion law data from Fickian behavior has not yet been reported in the literature, to our knowledge. A new statistical model and hypothesis test were developed here for this purpose. These are described in ESI† along with the results of this analysis. The results suggest that all three dyes exhibit Fickian-like diffusion (i.e.,  $\tau_0$  is not statistically different from

zero) in all samples investigated. While the  $\alpha$  values reported above suggest different contributions from 1D and 3D diffusion, the diffusion law analysis provides no evidence of domain-confined diffusion.<sup>28,29,46</sup> However, dye motion may actually be confined on length scales too small to detect under diffraction-limited conditions.<sup>31</sup> Note that the LLC correlation length reported above (170 nm) is of similar size to the confocal detection region and suggests that a few (i.e.  $< 10$ ) ordered domains are probed in each measurement. These results suggest that all three dyes can diffuse between the organized domains and are not strongly confined by the boundaries between them. They are also consistent with the apparent observation of mixed 1D diffusion within the domains and 3D diffusion between them.

The  $D_{Law}$  values obtained, however, do afford additional evidence of differences in the diffusion mechanisms of the three dyes. In this case, the diffusion law plots were reanalyzed with  $\tau_0 = 0$  (not shown). Figures 5b and 5c plot the mean  $D_{Law}$  values obtained. Data from  $\text{NRSO}_3^-$  are plotted separately from the other two dyes (see Figure 5c) to better highlight the differences in its behavior with  $\text{C}_{12}\text{EO}_{10}$  concentration. A comparison of the  $D_{Law}$  values for all three dyes reveals that they are of similar magnitude, as is consistent with the conclusion that the three dyes explore similar environments within the gels (see ESI†). However, a more detailed inspection of the data reveals obvious differences in the  $D_{Law}$  values. First,  $\text{NRC}_{14}$  exhibits the smallest  $D_{Law}$  at all gel concentrations, indicating it diffuses most slowly through the gels. NR exhibits modestly larger  $D_{Law}$  values, consistent with its smaller size. Indeed, data obtained for these two dyes in pure ethanol (see ESI†) reveal that  $D_{Law}$  is 34% smaller for  $\text{NRC}_{14}$  than for NR in homogeneous bulk solution. Interestingly, NR and  $\text{NRC}_{14}$  appear to exhibit inverted trends in  $D_{Law}$  with gel concentration. NR diffusion appears to be fastest at both low and high gel concentrations and slower at intermediate concentrations. In contrast,  $\text{NRC}_{14}$  appears to be

fastest at intermediate gel concentrations and slower at low and high concentrations. These apparent trends are difficult to explain at present and suggest that their rates of diffusion within the gels may be impacted by several different factors.

Particularly interesting are the data obtained from  $\text{NRSO}_3^-$ , which exhibit a clear monotonic trend to smaller values of  $D_{Law}$  with increasing gel concentration, as shown in Figure 5c). This trend is attributed to the greater preference of  $\text{NRSO}_3^-$  for the more polar corona regions of the gel. The dimensionality of  $\text{NRSO}_3^-$  diffusion may be mostly 3D, as suggested by its larger  $\alpha$  values (Figure 5a). However, the micelle cores could act as obstacles that confine its motion. As the density of micelles increases,  $D_{Law}$  would become smaller as a result. The data shown in Figure 5c are consistent with such behavior.

## Conclusions

Variable-area FCS methods were employed to explore the diffusion rates and mechanisms of three Nile red dyes serving as hydrophilic ( $\text{NRSO}_3^-$ ), hydrophobic ( $\text{NRC}_{14}$ ), and intermediate polarity (NR) probes of nanostructured hexagonal  $\text{C}_{12}\text{EO}_{10}$  LLC mesophases. The autocorrelation data obtained were analyzed using a model for anomalous 3D diffusion. The results revealed that NR exhibited the most anomalous diffusion, while  $\text{NRSO}_3^-$  was least anomalous and  $\text{NRC}_{14}$  exhibited intermediate behavior. These observations were interpreted to reflect increased occurrence of 1D diffusion in this case of NR due to its greater partitioning into 1D micelle core regions. In contrast,  $\text{NRSO}_3^-$  diffusion likely involves passage through the interconnected micelle corona regions in which it could more readily diffuse in 3D. Indeed,  $\text{NRSO}_3^-$  yielded a clear monotonic decrease in  $D_{Law}$  with increasing gel concentration and micelle density, consistent with confinement of its motions within the gels by the hydrophobic micelle cores. In contrast,  $\text{NRC}_{14}$  yielded the smallest  $D_{Law}$  values at the gel concentrations

examined, suggesting its larger size and interactions with the micelle cores slowed its motions. A diffusion law analysis revealed no evidence of domain-confined diffusion on sub-micron length scales for any of the three dyes at the gel concentrations investigated. These results are consistent with dye diffusion occurring by Fickian-like 1D and 3D mechanisms whose contributions vary between the dyes and with gel concentration with the C<sub>12</sub>EO<sub>10</sub> LLCs.

### **Author Contributions**

OS: investigation, formal analysis, visualization, validation, writing - original draft, and writing - review and editing; SGJ: investigation, formal analysis, visualization; TI: conceptualization, investigation, formal analysis, funding acquisition, supervision, writing - original draft, and writing - review and editing; DAH: conceptualization, investigation, formal analysis, visualization, funding acquisition, supervision, writing - original draft, and writing - review and editing.

### **Conflicts of Interest**

There are no conflicts to declare.

### **Acknowledgements**

The authors acknowledge the Division of Chemical Sciences, Geosciences, and Biosciences, Office of Basic Energy Sciences of the U.S. Department of Energy (DE-SC0002362) for partial support of this work. Parts of this work were carried out in the Characterization Facility, University of Minnesota, which receives partial support from the NSF through the MRSEC (Award Number DMR-2011401) and the NNCI (Award Number ECCS-2025124) programs. NSF is also thanked for providing the NMR used in characterizing dye structures in these studies (CHE-1826982). Eric Higgins is thanked for providing the C++

program used to autocorrelate the photon time-stamping data. Duy Hua is thanked for his help with the synthesis of the NR derivatives. Huafang Fan and Herman Coceancigh are thanked for collecting their NMR spectra, and Shu Jia is thanked for acquiring their mass spectra. Hamid Rashidi and Lianjie Xue are thanked for their help with data analysis and interpretation.

### †Electronic Supplementary Information.

Electronic supplementary information (ESI) available. See DOI:

<https://doi.org/10.1039/XXXXXX>

### References

- (1) Seliktar, D. Designing Cell-Compatible Hydrogels for Biomedical Applications. *Science* **2012**, *336*, 1124-1128.
- (2) Elstad, N. L.; Fowers, K. D. OncoGel (ReGel/Paclitaxel) - Clinical Applications for a Novel Paclitaxel Delivery System. *Adv. Drug Del. Rev.* **2009**, *61*, 785-794.
- (3) Escobar-Chavez, J. J.; Lopez-Cervantes, M.; Naik, A.; Kalia, Y. N.; Quintanar-Guerrero, D.; Ganem-Quintanar, A. Applications of Thermo-Reversible Pluronic F-127 Gels in Pharmaceutical Formulations. *J. Pharm. Pharmaceut. Sci.* **2006**, *9*, 339-358.
- (4) Zhou, M.; Kidd, T. J.; Noble, R. D.; Gin, D. L. Supported Lyotropic Liquid-Crystal Polymer Membranes: Promising Materials for Molecular-Size -Selective Aqueous Nanofiltration. *Adv. Mater.* **2005**, *17*, 1850-1853.
- (5) Ulbricht, M. Advanced Functional Polymer Membranes. *Polymer* **2006**, *47*, 2217-2262.
- (6) Dellinger, T. M.; Braun, P. V. Lyotropic Liquid Crystals as Nanoreactors for Nanoparticle Synthesis. *Chem. Mater.* **2004**, *16*, 2201-2207.
- (7) Wang, C.; Chen, D.; Jiao, X. Lyotropic Liquid Crystal Directed Synthesis of Nanostructured Materials. *Sci. Technol. Adv. Mater.* **2009**, *10*, 023001.
- (8) Constantin, D.; Oswald, P.; Imperor-Clerc, M.; Davidson, P.; Sott, P. Connectivity of the Hexagonal, Cubic, and Isotropic Phases of C12EO6/H2O Lyotropic Mixture Investigated by Tracer Diffusion and X-ray Scattering. *J. Phys. Chem. B* **2011**, *105*, 668-673.
- (9) Sakya, P.; Seddon, J. M.; Templer, R. H.; Mirkin, R. J.; Tiddy, G. J. T. Micellar Cubic Phases and Their Structural Relationships: The Nonionic Surfactant System, C12EO12/Water. *Langmuir* **1997**, *13*, 3706-3714.
- (10) Padia, F.; Yaseen, M.; Gore, B.; Rogers, S.; FBell, G.; Lu, J. R. Influence of Molecular Structure on the Size, Shape, and Nanostructure of Nonionic C(n)E(m) Surfactant Micelles. *J. Phys. Chem. B* **2014**, *118*, 179-188.
- (11) Zulauf, M.; Weckström; Hayter, J. B.; Degiorgio, V.; Corti, M. Neutron Scattering Study of Micelle Structure in Isotropic Aqueous Solutions of Poly(oxyethylene) Amphiphiles. *J. Phys. Chem.* **1985**, *89*, 3411-3417.

- (12) Mitchell, J. D.; Tiddy, G. J. T.; Waring, L.; Bostock, T.; McDonald, M. P. Phase Behavior of Polyoxyethylene Surfactants with Water. *J. Chem. Soc. Farad. Trans. I* **1983**, *79*, 975-1000.
- (13) Lin, Z.; Scriven, L. E.; Davis, H. T. Cryogenic Electron Microscopy of Rodlike or Wormlike Micelles in Aqueous Solutions of Nonionic Surfactant Hexaethylene Glycol Mono-hexadecyl Ether. *Langmuir* **1992**, *8*, 2200-2205.
- (14) Bernheim-Groswasser, A.; Wachtel, E.; Talmon, Y. Micellar Growth, Network Formation, and Criticality in Aqueous Solutions of the Nonionic Surfactant C12E5. *Langmuir* **2000**, *16*, 4131-4140.
- (15) Johansson, L.; Hedberg, P.; Löfroth, J.-E. Diffusion and Interaction in Gels and Solution. 5. Nonionic Micellar Systems. *J. Phys. Chem.* **1993**, *97*, 747-755.
- (16) Alexander, N. P.; Phillips, R. J.; Dungan, S. R. Multicomponent Diffusion In Aqueous Solutions of Nonionic Micelles and Decane. *Langmuir* **2019**, *35*, 13595-13606.
- (17) Alexander, N. P.; Phillips, R. J.; Dungan, S. R. Multicomponent Diffusion of Interacting, Nonionic Micelles with Hydrophobic Solutes. *Soft Matter* **2021**, *17*, 531-542.
- (18) Yethiraj, A.; Capitani, D.; Burlinson, N. E.; Burnell, E. E. An NMR Study of Translational Diffusion and Structural Anisotropy in Magnetically Alignable Nonionic Surfactant Mesophases. *Langmuir* **2005**, *21*, 3311-3321.
- (19) Gaemers, S.; Bax, A. Morphology of Three Lyotropic Liquid Crystalline Biological NMR Media Studied by Translational Diffusion Anisotropy. *J. Am. Chem. Soc.* **2001**, *123*, 12343-12352.
- (20) Elson, E. L.; Magde, D. Fluorescence Correlation Spectroscopy. I. Conceptual Basis and Theory. *Biopolymers* **1974**, *13*, 1-27.
- (21) Magde, D.; Elson, E.; Webb, W. W. Thermodynamic Fluctuations in a Reacting System - Measurement by Fluorescence Correlation Spectroscopy. *Phys. Rev. Lett.* **1972**, *29*, 705-708.
- (22) Aragon, S. R.; Pecora, R. Fluorescence Correlation Spectroscopy as a Probe of Molecular Dynamics. *J. Chem. Phys.* **1976**, *64*, 1791-1803.
- (23) Hess, S. T.; Huang, S.; Heikal, A. A.; Webb, W. W. Biological and Chemical Applications of Fluorescence Correlation Spectroscopy: A Review. *Biochemistry* **2002**, *41*, 697-705.
- (24) Elson, E. L. Fluorescence Correlation Spectroscopy: Past, Present, Future. *Biophys. J.* **2011**, *101*, 2855-2870.
- (25) Koyov, K.; Butt, J.-J. Fluorescence Correlation Spectroscopy in Colloid and Interface Science. *Curr. Opin. Coll. Interf. Sci.* **2012**, *17*, 377-387.
- (26) Wöll, D. Fluorescence Correlation Spectroscopy in Polymer Science. *RSC Adv.* **2014**, *4*, 2447-2465.
- (27) Masuda, A.; Ushida, K.; Okamoto, T. New Fluorescence Correlation Spectroscopy Enabling Direct Observation of Spatiotemporal Dependence of Diffusion Constants as an Evidence of Anomalous Transport in Extracellular Matrices. *Biophys. J.* **2005**, *88*, 3584-3591.
- (28) Wawrezynieck, L.; Rigneault, H.; Marguet, D.; Lenne, P.-F. Fluorescence Correlation Spectroscopy Diffusion Laws to Probe the Submicron Cell Membrane Organization. *Biophys. J.* **2005**, *89*, 4029-4042.
- (29) Veerapathiran, S.; Wohland, T. The Imaging FCS Diffusion Law in the Presence of Multiple Diffusive Modes. *Methods* **2018**, *140-141*, 140-150.

- (30) Gupta, A.; Phang, I. Y.; Wohland, T. To Hop or Not to Hop: Exceptions in the FCS Diffusion Law. *Biophys. J.* **2020**, *118*, 2434-2447.
- (31) Sachl, R.; Bergstrand, J.; Widengren, J.; Hof, M. Fluorescence Correlation Spectroscopy Diffusion Laws in the Presence of Moving Nanodomains. *J. Phys. D: Appl. Phys.* **2016**, *49*, 114002.
- (32) Hungerford, G.; Castanheira, E. M. S.; Real Oliveira, M. E. C. D.; da Graca Miguel, M.; Burrows, H. D. Monitoring Ternary Systems of C12E5/Water/Tetradecane via the Fluorescence of Solvatochromic Probes. *J. Phys. Chem. B* **2002**, *106*, 4061-4069.
- (33) Stuart, M. C. A.; van de Pas, J. C.; Engberts, J. B. F. N. The Use of Nile Red to Monitor the Aggregation Behavior in Ternary Surfactant-Water-Organic Solvent Systems. *J. Phys. Org. Chem.* **2005**, *18*, 929-934.
- (34) Dong, R.; Hao, J. Complex Fluids of Poly(oxyethylene) Monoalkyl Ether Nonionic Surfactants. *Chem. Rev.* **2010**, *110*, 4978-5022.
- (35) Martin-Brown, S. A.; Fu, Y.; Saroja, G.; Collinson, M. M.; Higgins, D. A. Single-Molecule Studies of Diffusion by Oligomer-Bound Dyes in Organically Modified Sol-Gel-Derived Silicate Films. *Anal. Chem.* **2005**, *77*, 486-494.
- (36) Lange, J. J.; Culbertson, C. T.; Higgins, D. A. Single Molecule Studies of Solvent-Dependent Diffusion and Entrapment in Poly(dimethylsiloxane) Thin Films. *Anal. Chem.* **2008**, *80*, 9726-9734.
- (37) Kirkeminde, A. W.; Torres, T.; Ito, T.; Higgins, D. A. Multiple Diffusion Pathways in Pluronic F127 Mesophases Revealed by Single Molecule Tracking and Fluorescence Correlation Spectroscopy. *J. Phys. Chem. B* **2011**, *115*, 12736-12743.
- (38) Kisley, L.; Brunetti, R.; Tauzin, L. J.; Shuang, B.; Yi, X.; Kirkeminde, A. W.; Higgins, D. A.; Weiss, S.; Landes, C. F. Characterization of Porous Materials by Fluorescence Correlation Spectroscopy Super-Resolution Optical Fluctuation Imaging. *ACS Nano* **2015**, *9*, 9158-9166.
- (39) Enderlein, J.; Gregor, I.; Patra, D.; Fitter, J. Art and Artefacts of Fluorescence Correlation Spectroscopy. *Curr. Pharm. Biotechnol.* **2004**, *5*, 155-161.
- (40) Enderlein, J.; Gregor, I.; Patra, D.; Dertinger, T.; Kaupp, U. B. Performance of Fluorescence Correlation Spectroscopy for Measuring Diffusion and Concentration. *Chem. Phys. Chem.* **2005**, *6*, 2324-2336.
- (41) Banachowicz, E.; Patkowski, A.; Meier, G.; Klamecka, K.; Gapinski, J. Successful FCS Experiment in Nonstandard Conditions. *Langmuir* **2014**, *30*, 8945-8955.
- (42) Molteni, M.; Ferri, F. Commercial Counterboard for 10 ns Software Correlator for Photon and Fluorescence Correlation Spectroscopy. *Rev. Sci. Instrum.* **2016**, *87*, 113108.
- (43) Hamley, I. W.; Castelletto, V. Small-Angle Scattering of Block Copolymers: in the Melt, Solution and Crystal States. *Progress Polym. Sci.* **2004**, *29*, 909-948.
- (44) Berthod, A.; Tomer, S.; Dorsey, J. G. Polyoxyethylene Alkyl Ether Nonionic Surfactants: Physicochemical Properties and Use for Cholesterol Determination in Food. *Talanta* **2001**, *55*, 69-83.
- (45) Widengren, J.; Mets, U.; Rigler, R. Fluorescence Correlation Spectroscopy of Triplet States in Solution: A Theoretical and Experimental Study. *J. Phys. Chem.* **1995**, *99*, 13368-13379.
- (46) Bag, N.; Ng, X. W.; Sankaran, J.; Wohland, T. Spatiotemporal Mapping of Diffusion Dynamics and Organization in Plasma Membranes. *Meth. Appl. Fluor.* **2016**, *4*, 034003.